Journal of Water Process Engineering 33 (2020) 101015

Contents lists available at ScienceDirect

Journal of Water Process Engineering

journal homepage: www.elsevier.com/locate/jwpe

Mechanistic insight of the formation of visible-light responsive nanosheet graphitic carbon nitride embedded polyacrylonitrile nanofibres for wastewater treatment

Nur Hashimah Alias[a,b], Juhana Jaafar[a,*], Sadaki Samitsu[c], A.F. Ismail[a], Mohamad Azuwa Mohamed[d], M.H.D. Othman[a], Mukhlis A. Rahman[a], Nur Hidayati Othman[b], N.A.M. Nor[a], N. Yusof[a], F. Aziz[a]

[a] Advanced Membrane Technology Research Centre (AMTEC), School of Chemical and Energy Engineering, Faculty of Engineering, Universiti Teknologi Malaysia, 81310 Skudai, Johor, Malaysia
[b] Department of Oil and Gas Engineering, Faculty of Chemical Engineering, Universiti Teknologi MARA, 40450 Shah Alam, Selangor, Malaysia
[c] Data-driven Polymer Design Group, Research and Services Division of Materials Data and Integrated System (MaDIS), National Institute for Materials Science (NIMS), 1-2-1 Sengen, Tsukuba, Ibaraki 305-0047, Japan
[d] Centre for Advanced Materials and Renewable Resources, Faculty of Science and Technology, Universiti Kebangsaan Malaysia, 43600 UKM Bangi, Selangor, Malaysia

ARTICLE INFO

Keywords:
Adsorption
Photocatalytic degradation
Graphitic carbon nitride
Nanofibres
Wastewater

ABSTRACT

Effective capture and in situ photodegradation of methylene blue (MB) dye is a promising technique to purify wastewater containing MB. With recently elicited ripples of discovery on graphitic carbon nitride (g-C_3N_4), this study investigates the performance of g-C_3N_4 on photodegradation of MB. In this study, polyacrylonitrile (PAN) nanofibres embedded with g-C_3N_4 photocatalyst was successfully prepared using electrospinning technique which produced liquid-permeable self-supporting photocatalytic nanofibre mats that can be handled easily. Different configurations of g-C_3N_4 were synthesised, bulk g-C_3N_4 (bg-C_3N_4) and nanosheets g-C_3N_4 (nsg-C_3N_4) from urea using a green facile template-free method. Effective photocatalytic activity of the g-C_3N_4 nanofibres was confirmed by 97.3% degradation of MB under visible light irradiation. Photodegradation of MB in aqueous solution by g-C_3N_4 nanofibres predominantly attributed to the synergetic effects of MB adsorption by PAN nanofibres and photocatalytic degradation of MB by g-C_3N_4 photocatalyst. This present work not only presents the simplest ecofriendly and economical approach to fabricate g-C_3N_4 nanofibre photocatalyst, but also paves new opportunities for this advanced photocatalyst as great potential in environmental remediation for treatment of industrial MB wastewater.

1. Introduction

Graphitic carbon nitride (g-C_3N_4) is one of the oldest material described in the chemical literature which has recently experienced renaissance as highly active photocatalyst. Previously [1,2] mentioned that historically in 1830s, Berzelius and Liebig have reported on the general formula of carbon nitride family as $(C_3N_3H)_n$ which traced in embryonic form 'melon', a linear polymer consisting of interconnected tri-s-triazines via secondary nitrogen. Meanwhile g-C_3N_4 in the form of 2D sheets consisting of tri-triazines interconnected via tertiary amines. Previous breakthrough studies have revealed several intrinsic features of g-C_3N_4. Previous breakthrough studies have revealed several intrinsic features of g-C_3N_4. Being a metal-free heterogeneous catalyst with simple constitution elements of C, N, and residual hydrogen in defects, the g-C_3N_4 is able to renders the materials nontoxic and biocompatible for some applications [3]. In addition, g-C_3N_4 shows onset on bandgap adsorption around 420 nm and exhibit strong blue photoluminescence at range of (430–550 nm) at room temperature. Most importantly, g-C_3N_4 owns a band gap of 2.7 eV that suitable as visible-light-active photoresponse photocatalyst with conductive band (CB) of -1.1 eV and valence band (VB) of +1.6 eV respectively, and normal hydrogen electrodes (NHEs) as reference [4]. With remarkable discovery on g-C_3N_4 that owns appealing electronic band gap, extraordinary physicochemical stability, facile synthesis, and earth-abundant nature [5–7], this study investigated the photodegradation capability of g-C_3N_4 on methylene blue (MB) in aqueous.

* Corresponding author.
E-mail address: juhana@petroleum.utm.my (J. Jaafar).

https://doi.org/10.1016/j.jwpe.2019.101015
Received 26 July 2019; Received in revised form 16 October 2019; Accepted 18 October 2019
Available online 20 November 2019
2214-7144/

Based on our previous works, the synthesised bulk g-C_3N_4 (bg-C_3N_4) was obtained as agglomerated powder [8], thus with reduced in effective surface area, it suffers from narrow visible light absorption range and high recombination probability of photogenerated charge carriers and finally limits its photocatalytic activity [9]. Therefore, to achieve high photocatalytic activity to irradiation, nanosheets graphitic carbon nitride (nsg-C_3N_4) was synthesised from bg-C_3N_4 using liquid exfoliation method [10]. Moreover, basic requirement to design and operate separation process requires a separation material that is easy to be handled. Therefore, electrospinning technique was employed in this study to fabricate a specific-shaped of g-C_3N_4 with high surface area made from polymer nanofibres composite. This technique can effectively dispersed nanoparticles photocatalyst into polymer-based nanofibres [11,12]. Recently, study by [13,14] have reported that addition of other materials through facile blending have improved the properties of polyacrylonitrile (PAN) nanofibres to generate composite nanofibres with synergistic properties. In this work, g-C_3N_4 was dispersed into PAN spinning solution to produce nonwoven mat of PAN nanofibres embedded with g-C_3N_4. Previous literature only reported on photodegradation of MB contaminant using g-C_3N_4 powder photocatalyst, but none has reported by using nsg-C_3N_4 embedded PAN nanofibres.

Dyeing industries, particularly textile industries utilise colour and massive amount of water during production operations [15]. There are several groups of dye such as basic, acidic, diazo, azo, metal-based dyes and anthraquinone-based, which pose a threat to environment and public health [16–20]. Therefore, decolorization and detoxification of dye-containing wastewater need to be conducted before discharging the wastewater into natural water bodies [21–23]. Physical and chemical methods including adsorption, membrane separation, precipitation and coalescence have conventionally been developed to treat MB from water and wastewater [18,24]. However, these methods only decrease the pollutant dye concentration in water and a non-destructive process. A substantial amount of research for the treatment and management on large amount of textile effluents such as methylene blue (MB) dye has rapidly been conducted to minimise its impact towards the environment [25,26]. Furthermore, removal of MB dye does not only become an important but challenging area of research for wastewater treatment. Therefore, the superior surface area and promising electronic properties rendered by the nanofibres embedded g-C_3N_4 is expected to improve the photocatalytic performance through synergetic effects of MB adsorption in nanofibre polymer matrix and in-situ photodegradation. As such, electrospun g-C_3N_4 nanofibres could be an alternatively feasible candidate for both adsorption and photocatalysis for dye wastewater treatment.

2. Experimental

2.1. Materials

The g-C_3N_4 powders were synthesised using urea (AR grade) and isopropanol (IPA) purchased from QReC Malaysia. Dimethylformamide (DMF, RCI Labscan) and polyacrylonitrile (PAN, 150,000 g/mol, Sigma Aldrich) were used as a solvent and polymer binder, respectively, for the electrospinning dope solution. Methylene blue (MB, Reag. Ph Eur) used in photocatalytic measurement was supplied by Sigma Aldrich. Fig. 1 illustrates the structure of MB. In this work, all the analytical reagent and chemicals were used without further purification. The reverse osmosis (RO) water used was from Millipore, ASTM Type III.

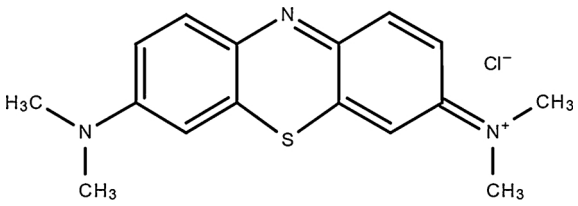

Fig. 1. Structure of methylene blue, MB [27].

2.2. Sample preparation

A green facile template-free method was employed to synthesise g-C_3N_4 powder as reported in our previous work [28,29]. Ten grams of urea powder was calcined at 500 °C at ambient atmosphere in an ashing furnace (AAF 1100 Carbolite) for 4 h at a heating rate of 5 °C/min. The as-synthesised bulk graphitic carbon nitride (bg-C_3N_4) powder in pale yellow was obtained and ground using a mortar. A sonication-assisted liquid exfoliation method was used to treat bg-C_3N_4 further to synthesise nanosheets graphitic carbon nitride (nsg-C_3N_4). A total of 100 mg bg-C_3N_4 powder was mixed with 100 mL of IPA as a dispersion solvent and further sonicated for 10 h. The solution was dried overnight in an oven at 80 °C to obtain light yellow powder, denoted as nsg-C_3N_4.

The electrospinning of dope solution was prepared using a method reported in a previous study [28]. A quantity of g-C_3N_4 was mixed with DMF before the solution was sonicated using an ultrasonicator (Delta Ultrasonic, DC150 H) for 5 h at 40 kHz. Next, 90 wt% of PAN powder was added into the mixture before it was sonicated homogenously for another 5 h. To fabricate PAN nanofibres containing g-C_3N_4, a nanofibres electrospinning unit (Progene Link Sdn. Bhd., NF-1000) was employed, and the experimental setup was illustrated in Fig. 2a. A 10 mL hypodermic syringe that was connected with a blunt tip metallic needle was filled with electrospinning dope solution and placed inside the electrospinning chamber where the flow rate of a syringe pump was set at 1 mL/h. The applied voltage for the electrospinning unit was set at 15 kV, and the tip-to-collector distance was set at 18 cm. The dope solution was electrospun on an aluminium collector and was peeled off manually after the electrospinning completed. The resulted nanofibres comprising bg-C_3N_4 and nsg-C_3N_4 were named as bulk graphitic carbon nitride nanofibres (NFbg-C_3N_4) and nanosheets graphitic carbon nitride nanofibres (NFnsg-C_3N_4), respectively.

2.3. Characterisation

The surface morphology of the samples was observed using field-

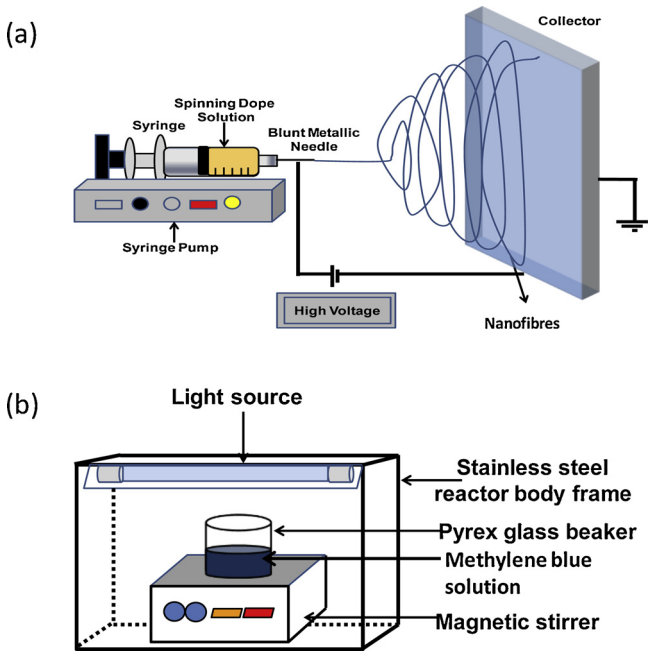

Fig. 2. (a) Experimental setup for electrospinning process of g-C_3N_4 embedded PAN nanofibres; (b) schematic diagram of the suspension photocatalytic reactor.

emission scanning electron microscopy (FESEM, Hitachi High-Tech. Co., Hitachi SU8020). The mean nanofibres diameter was analysed using Gaussian function approximation by Origin software. Transmission electron microscopy was performed using HR–TEM (Hitachi High-Tech. Co., Hitachi HT7700) under 120 kV voltage acceleration. Nitrogen adsorption/desorption measurement at −196 °C was performed using an automatic gas adsorption instrument (BEL Japan, Belsorp-max). Brunauer–Emmett–Teller (BET) and Barrett–Joyner–Halenda (BJH) methods were used to obtain the specific surface area (S_{BET}) and pore size distributions of the samples, respectively.

The chemical structures of the samples were characterised using Fourier transform infrared spectroscopy (FTIR, JASCO Inc., FT/IR-6100) with absorbance configuration. UV–visible–NIR spectrophotometer (Shidmadzu Co., UV-3101PC) was used to record the absorption spectra of the g-C_3N_4. The obtained reflectance values were converted to absorbance based on Kubelka–Munk function equation. Photoluminescence analysis (JASCO Inc., FP-6500) was employed to record the photoluminescence spectra of the g-C_3N_4. The g-C_3N_4 were excited under illumination at 360 nm, and the emission spectra were recorded from 350 to 750 nm including the peak wavelength of the excitation light. Software provided by JASCO Inc. was used to calculate the photoluminescence efficiency.

2.4. Photocatalysis measurement

An aqueous solution of methylene blue (MB) was freshly prepared at 10 ppm. Fig. 2b shows the suspension mode photocatalytic reactor that was used to conduct all the photocatalytic measurements. A 450 mL beaker containing suspension solution was placed inside the photocatalytic reactor at 15 cm distance from the source of light. A suspension solution was prepared by adding 0.20 g of photocatalyst in 200 mL of MB solution. During photocatalytic activity, a white light-emitting diode (LED) lamp (30 W) was used as a source of visible light with a wavelength region of > 420 nm. Air bubbles were continuously supplied using an air diffuser to ensure adequate supply of oxygen to the reaction. The suspension solution was stirred for 60 min in the dark to ensure adsorption equilibrium before irradiation. At every 30 min interval during irradiation, 5 mL of suspension was collected to measure the absorbance using UV–vis spectrophotometer (Hach, DR5000). The MB concentration was determined based on the absorbance value of MB recorded at 662 nm. The photocatalytic activity is expressed in the percentage MB removal according to Eq. (1),

$$\text{MB removal efficiency}\,(\%) = \frac{C_o - C_t}{C_o} \times 100 \quad (1)$$

where C_o is the initial absorbance of the suspension solution and C_t is the absorbance at time of 0–300 min is.

3. Results and discussion

3.1. Characterisation of g-C_3N_4 powders and g-C_3N_4/PAN nanofibres

Fig. 3 shows the SEM and TEM images of the as-synthesised bg-C_3N_4 and nsg-C_3N_4. It can be clearly seen that bg-C_3N_4 is a porous particle with a pore size of approximately 0.1–2 μm (Fig. 3a). The TEM images confirm the porous structure of bg-C_3N_4 based on its edge regions which exhibit a relatively dark brightness (Fig. 3b). The formation of this porous structure was due to decomposition of urea which generated gas bubbles during thermal treatment. The existence of this porous structure is favourable as it facilitates high surface area and accommodates numerous channels to enable mass diffusion to enhance separation processes [2]. Meanwhile, the SEM image of nsg-C_3N_4 presented in Fig. 3c shows a flower-like structure of thin graphitic nanosheet layers embedded in open pores. In addition, two-dimensional (2D) layers of g-C_3N_4 with laminar morphology like silk veil that nearly transparent than bg-C_3N_4 is presented in the TEM images of nsg-C_3N_4 (Fig. 3d). Thus, these findings prove that sonication-assisted liquid exfoliation performed on bg-C_3N_4 successfully exfoliated its bulk structure to form nsg-C_3N_4.

Polymer nanofibre was embedded with g-C_3N_4 using electrospinning to produce g-C_3N_4/PAN nanofibre mats with high surface area and easy to handle manually. PAN polymer was selected as a polymer matrix for nanofibres because it has no optical absorbance in visible light region. Furthermore, owing a similar molecular structure with that of g-C_3N_4, PAN polymer is favourable for dispersion and miscibility with g-C_3N_4. Electrospinning technique successfully generated nanofibers containing g-C_3N_4 powder, as shown in the SEM images in Fig. 4a and b for NFng-C_3N_4 and NFnsg-C_3N_4, respectively. Interestingly, the electrospun nanofibre mats have a network of a highly well interconnected open pore structure in several micrometre size. Furthermore, the noduleless structure of nanofibres formed indicates a uniform distribution of g-C_3N_4 along the PAN nanofibres surface. The electrospun fibre formed was also straight with an average diameter in nanometre size. The mean nanofibre diameters for NFbg-C_3N_4 and NFnsg-C_3N_4 were also examined using digital imaging analysis of the SEM images, where the mean nanofibre diameters for NFbg-C_3N_4 and NFnsg-C_3N_4 were 207 ± 2 and 262 ± 6 nm, respectively. In comparison to smooth straight shape of PAN nanofibres, NFbg-C_3N_4 have numerous lumps on the smooth nanofibres shape. These spherical lumps with a few micrometre size corresponded to the bulky shape of bg-C_3N_4 embedded in the nanofibres. In contrast, due to the successful exfoliation of bulky bg-C_3N_4 to form thin nanosheets of nsg-C_3N_4, NFnsg-C_3N_4 had less numbers of thin lumps compared to NFbg-C_3N_4 indicating that nsg-C_3N_4 were uniformly distributed along the PAN nanofibres surface [28,29]. These uniform, smooth, and straight in infinite length structure of NFnsg-C_3N_4 produced a slightly higher mean nanofibre diameter of NFnsg-C_3N_4 compared to NFbg-C_3N_4.

Table 1 summarises the results of S_{BET}, total pore volume, and mean pore diameter of bg-C_3N_4 and nsg-C_3N_4 measured via nitrogen adsorption/desorption isotherms. The S_{BET} of bg-C_3N_4 is 41.3 m^2/g which is slightly higher than that of nsg-C_3N_4 (36.7 m^2/g). Most likely, the lower S_{BET} after exfoliation might be due to the lower recovery of g-C_3N_4 layer-restacking during the drying process of nsg-C_3N_4. However, after exfoliation, the total pore volume and mean pore diameter of g-C_3N_4 increased. Thus, enhancement in pore volume and size improved the characteristic for nsg-C_3N_4 for better adsorption properties.

Fig. 5 presents the FTIR spectra of bg-C_3N_4 and nsg-C_3N_4. The typical peaks of the spectra obtained were consistent with those of g-C_3N_4 reported elsewhere [30,31]. Generally, the obtained spectra of nsg-C_3N_4 matched the spectra of bg-C_3N_4, indicating similar chemical structures and confirming that the exfoliation process did not involve any reaction. The sharp band at 810 cm^{-1} corresponds to the condensed CN heterocycles which originated from breathing of the tri-s-triazine units ring. The absorption bands at 1568 and 1630 cm^{-1} correspond to the C≡N stretching, while the three bands around 1253, 1326 and 1417 cm^{-1} are attributed to the C—N stretching. The peaks at 900–1800 cm^{-1} are mainly attributed to the aromatic CN heterocycles which contain either trigonal N(–C)$_3$ as fully condensed or bridging C—NH—C units as partially condensed [30,32]. Meanwhile, under broad shoulder of 3000–3500 cm^{-1}, the two weak peaks at 3176 and 3329 cm^{-1} correspond to the stretching modes of uncondensed amine groups, –NH_2 or = NH. Overall, these FTIR results suggest that g-C_3N_4 units mainly consist of various chemical bonds made from C and N atoms such as C—N bond, C≡N bond, N(–C)$_3$, and C—NH—C bridges.

The electronic structures of bg-C_3N_4 and nsg-C_3N_4 are presented by UV–vis absorption shown in Fig. 6. Comparing the two g-C_3N_4 (Fig. 6a), the diffuse reflectance spectra of nsg-C_3N_4 exhibited a red shift of absorption wavelength. The increase in red shift of 10 nm absorption under visible light region promoted the generation of more electron–hole pairs under sunlight irradiation, thus improving the photocatalytic activity of nsg-C_3N_4 [33]. The Kubelka–Munk function was used to

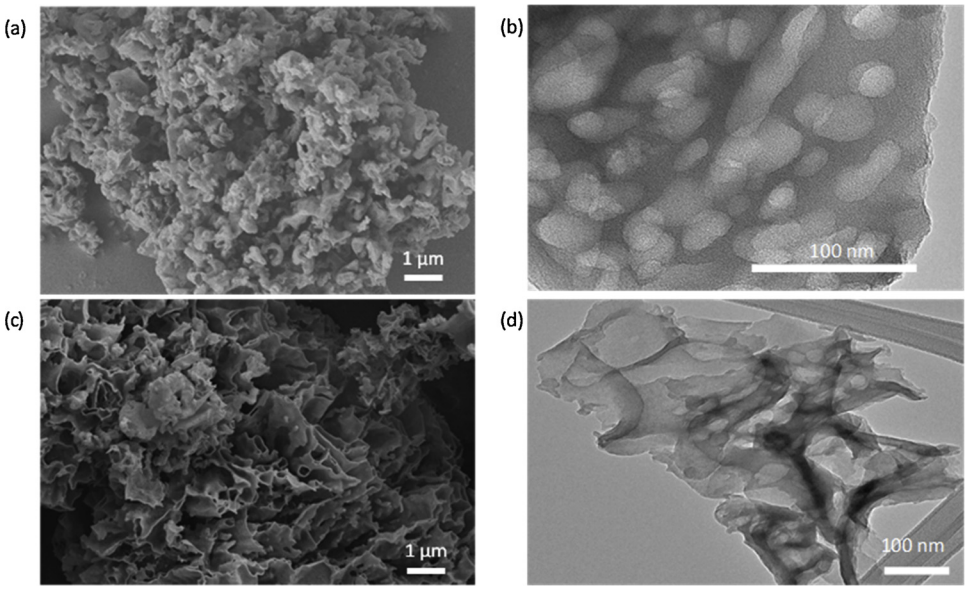

Fig. 3. Morphological characterisations of (a and b) bg-C_3N_4 and (c and d) nsg-C_3N_4 performed using (a and c) SEM and (b and d) TEM, respectively.

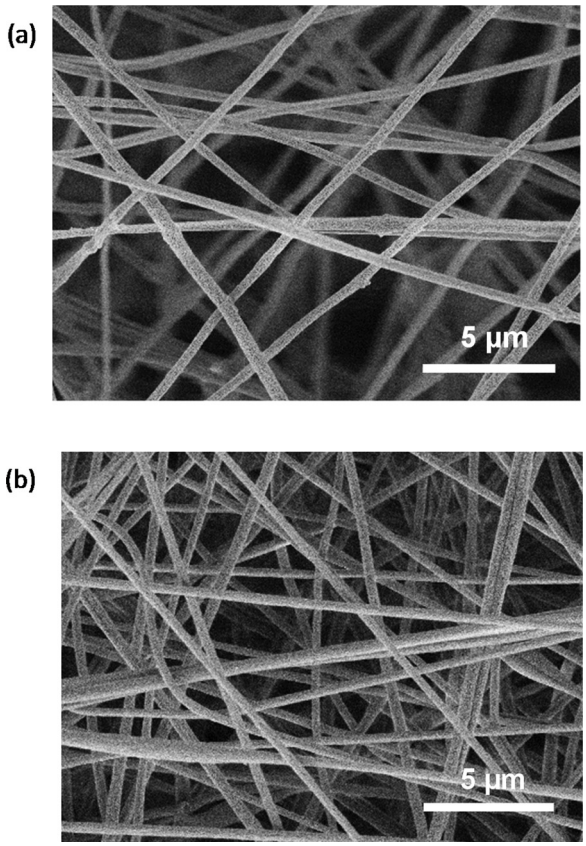

Fig. 4. SEM images of (a) NFbg-C_3N_4 and (b) NFnsg-C_3N_4.

estimate the band gap energy of the samples by plotting $(\alpha h\upsilon)^2$ versus $h\upsilon$, where α is the absorption coefficient and $h\upsilon$ is the photon energy [34]. Based on the intercept of the tangent plot, it is estimated that the band gap energies were 2.72 and 2.68 eV for bg-C_3N_4 and nsg-C_3N_4, respectively (Fig. 6b). Therefore, the resulted red shift in absorption spectra was attributed by the band gap energy narrowing of 0.04 eV which certainly suggests that the exfoliation of bg-C_3N_4 affected the electronic properties of g-C_3N_4.

It is well acknowledged that photoluminescence (PL) emission

Table 1
Structural and band gap properties of bg-C_3N_4, nsg-C_3N_4, NFbg-C_3N_4, and NFnsg-C_3N_4.

Sample	bg-C_3N_4	nsg-C_3N_4	NF bg-C_3N_4	NF nsg-C_3N_4
S_{BET} ($m^2 \cdot g^{-1}$)	41.3	36.7	15.4	13.3
V_{total} ($cm^3 \cdot g^{-1}$)	0.21	0.25	0.08	0.09
d_m (nm)	20.8	26.7	N.A.†	N.A.†
E_g (eV)	2.72	2.68	–	–

S_{BET}: BET surface area, V_{total}: total pore volume: d_m: mean pore diameter: E_g: band gap: ϕ: PL efficiency: †N.A.:the mean pore diameter could not be determined due to the very low pore volume of the nanofibres.

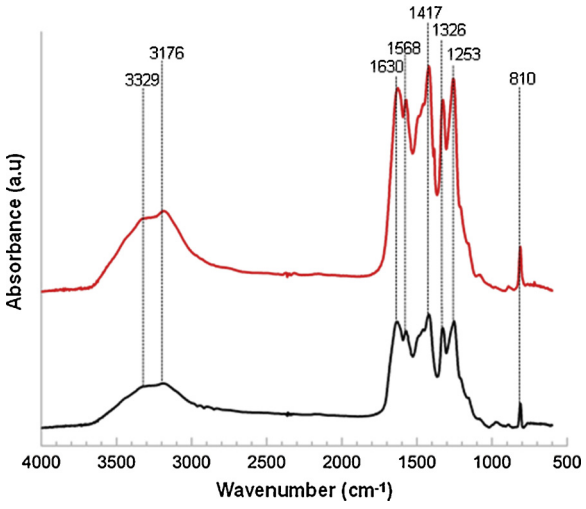

Fig. 5. FTIR spectra for bg-C_3N_4 (black line) and nsg-C_3N_4 (red line).

originates from electron recombination [35]. Therefore, PL intensity was used to reflect the photocatalyst separation efficiency to assess the catalytic function. The PL spectra of g-C_3N_4 comprise a broad peak at 400–650 nm with the peak maximum observed at 448 nm (Fig. 6c).The

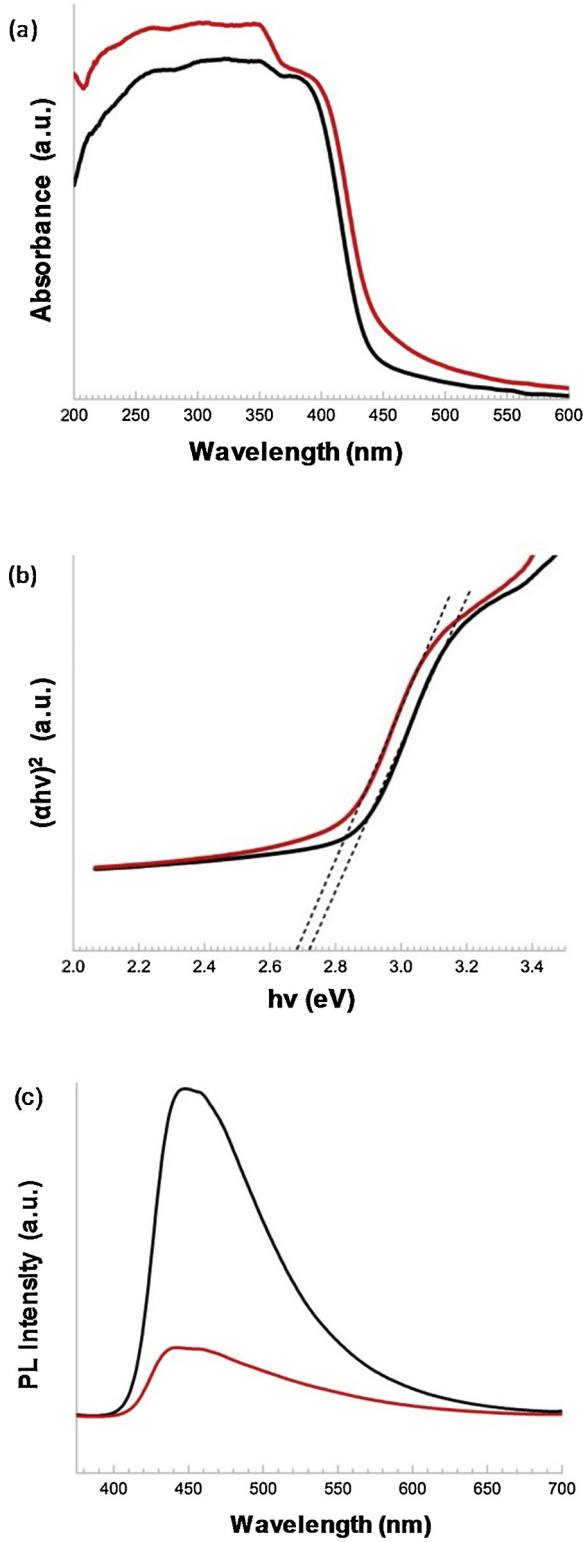

Fig. 6. (a) UV–vis absorption spectra, (b) Kubelka–Munk function for estimating the band gap energy, (c) photoluminescence (PL) spectra of bg-C_3N_4 (black line) and nsg-C_3N_4 (red line).

shape of PL spectra for bg-C_3N_4 is almost same with that for nsg-C_3N_4, however the peak intensity of nsg-C_3N_4 is much smaller than that of bg-C_3N_4. Based on integral sphere assembly, PL quantum efficiency of the g-C_3N_4 samples was quantitatively determined and the efficiency of nsg-C_3N_4 was 1.0%, which is one-third of that of bg-C_3N_4 (3.1%). These promising results prove that nsg-C_3N_4 has higher photocatalytic activity due to the disturbance of electron–hole recombination.

From nitrogen adsorption measurement, the S_{BET} values of NFbg-C_3N_4 and NFnsg-C_3N_4 were 15.4 and 13.3 m^2/g, respectively. The S_{BET} values of nanofibres were much smaller compared to that of g-C_3N_4. Most likely, the S_{BET} values of nanofibres were only contributed by the outer surface of PAN nanofibres, not by g-C_3N_4 embedded into the PAN matrix. Therefore, to verify these hypotheses, we calculated the geometric surface area of nanofibres using Eq. 2 where A is the area of the nanofibres, V is the volume, ρ is the density of PAN, d is the diameter of the nanofibres, L is the length, and S is the specific surface area.

$$S = \frac{A}{\rho V} = \frac{\pi dL}{\rho \frac{\pi d^2}{4} L} = \frac{4}{\rho d} \tag{2}$$

By using the values of S_{BET}, 15.4 m^2/g for bg-C_3N_4 and 13.3 m^2/g for nsg-C_3N_4, and ρ of 1.18 g/cm^3 [36], the calculated average diameter of nanofibre was 220 nm for bg-C_3N_4 and 255 nm for nsg-C_3N_4. These calculated diameters are similar with the mean diameter obtained from the digital image analysis of the SEM images. Therefore, this evidence suggests that the S_{BET} value only represents the surface area of nanofibres surface, but not the porous structure of g-C_3N_4. This finding is possibly due to the porous g-C_3N_4 encapsulated in the matrix of PAN polymer. Meanwhile, the total pore volumes of NFbg-C_3N_4 and NFnsg-C_3N_4 were much lower than that of g-C_3N_4, which is attributed to the less dense stacking of nanofibres to form nanopores which were accessible by a gas adsorption measurement (pore size smaller than 200 nm).

The FTIR spectra of NFbg-C_3N_4, NFnsg-C_3N_4, and PAN nanofibres are shown in Fig.7. The characteristic peaks of PAN exist in both NFbg-C_3N_4 and NFnsg-C_3N_4 spectra such as the stretching vibration of nitrile group (–CN–) at 2242 cm^{-1} and the stretching vibration and bending vibration of methylene (−CH_2–) at 2936 and 1453 cm^{-1} [37]. The weight ratio of PAN to g-C_3N_4 of 10:1 explains that the nanofibres were mostly made of the PAN polymer matrix. Other than the peaks of PAN, the characteristic peaks of g-C_3N_4 were found at 810 cm^{-1} (aromatic CN heterocycles), 1243 and 1320 cm^{-1} (C—N stretching), 1563 cm^{-1} and 1621 cm^{-1} (C≡N stretching), and 3000–3380 cm^{-1} (amine groups, –NH_2 or = NH), which confirm that g-C_3N_4 was successfully embedded into the PAN polymer matrix. These electrospun nanofibres, NFbg-C_3N_4 and NFnsg-C_3N_4 have the excellent features of large surface area and defined open pores which could facilitate mass diffusion and rapid adsorption of targeted pollutant molecules. Furthermore, uniform dispersion of g-C_3N_4 embedded into the PAN polymer matrix would help to promote vast numbers of active sites for effective interactions between the reactant and photocatalyst and finally improves the

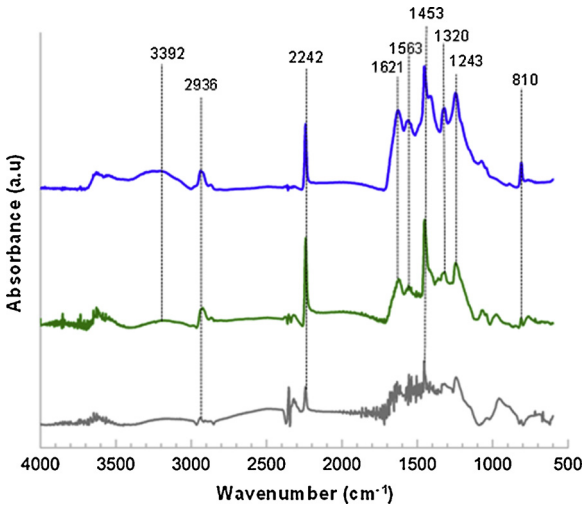

Fig. 7. FTIR spectra of NFbg-C_3N_4 (blue line), NFnsg-C_3N_4 (green line), and PAN nanofibres (grey line).

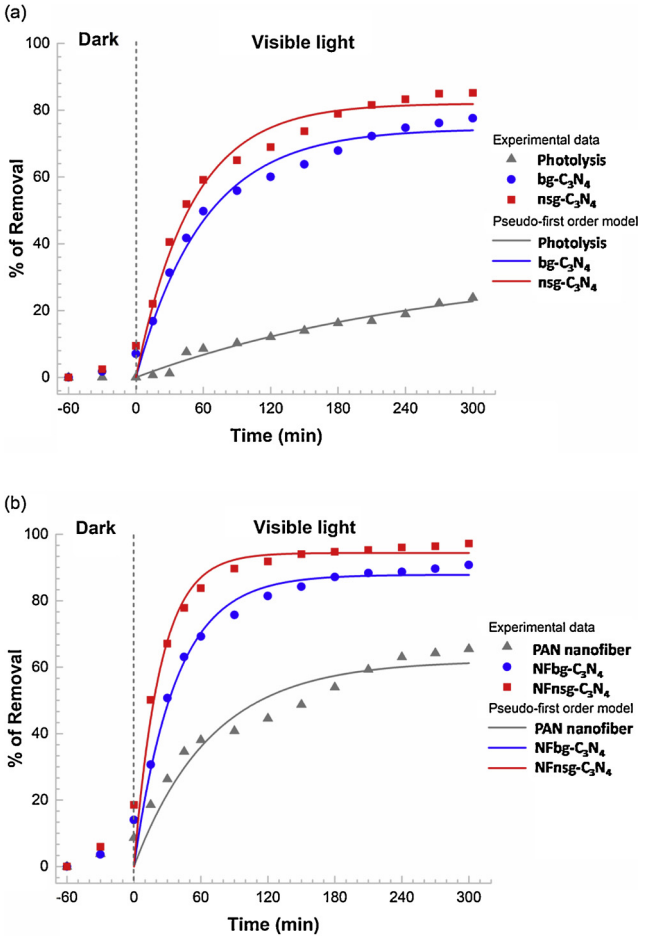

Fig. 8. Removal of MB under dark condition and visible light illumination, and nonlinearised pseudo-first-order kinetic photodegradation model for (a) photolysis, bg-C_3N_4, and nsg-C_3N_4, and (b) PAN nanofibre, NFbg-C_3N_4, and NFnsg-C_3N_4.

photocatalytic activity.

3.2. Photodegradation of methylene blue (MB)

The removal efficiency of MB was investigated using MB solution with the initial concentration of 10 ppm. The removal efficiency of MB was measured based on adsorption and photocatalytic degradation of MB solution. Before irradiation, the mixture of MB and photocatalyst was stirred for 60 min in the dark to achieve adsorption equilibrium and to make sure that adsorption reading does not interfere with the reading of photocatalytic degradation of MB. Therefore, when the suspension of photocatalyst and MB solution was irradiated with light, the removal of MB is specifically referred to the photocatalytic degradation. The photocatalytic activity of g-C_3N_4 on MB was observed under visible light irradiation ($\lambda > 420$ nm).

Fig. 8a shows the photodegradation removal of MB with the presence of bg-C_3N_4 and nsg-C_3N_4 powder under visible light for 300 min, with samples collected at an interval of 30 min. Photolysis was conducted to evaluate the stability of MB solution under visible light irradiation without the presence of photocatalyst. The direct decomposition of MB in the absence of photocatalyst was not detected. About 23.9% of MB was decomposed under visible light illumination after 300 min without the presence of photocatalyst. In general, the rapid increase in degradation just after visible light was activated indicates the effective photodegradation by g-C_3N_4. The incorporation of bg-C_3N_4 decreased 10% of te MB concentration under dark condition, which indicates that bg-C_3N_4 can adsorb the MB due to porous structure. The bg-C_3N_4 illuminated with visible light effectively decomposed 77.6% of MB after 300 min. The result reveals photocatalytic activity of bg-C_3N_4 under visible light illumination. The degradation of MB by nsg-C_3N_4 was 85.1%, which is higher than that by bg-C_3N_4 that might be due to the narrowed band gap and improved photoresponse of nsg-C_3N_4 implying better photocatalytic activity on MB. The obtained nsg-C_3N_4 changed in colour from light yellow (bg-C_3N_4) to brown yellow corresponding to the expanded adsorption in visible light region [38], thus narrowed the band gap and improved light absorbance that is useful for photocatalytic performance. Moreover, the higher adsorption capacity and photocatalytic degradation efficiency of nsg-C_3N_4 may originate from a well-dispersed nsg-C_3N_4 in MB aqueous solution by electrostatic repulsive interaction [30].

The photocatalytic degradation of MB might be due to the absorption of photon energy by nsg-C_3N_4 that caused electron excitation from valence band (VB) to conduction band (CB), leaving the positive holes at VB. According to [39], nsg-C_3N_4 was unable to generate hydroxyl radicals ($^{\cdot}OH$) for MB degradation due to less positive VB position of nsg-C_3N_4 compared to the standard redox potential ($OH^-/^{\cdot}OH = +1.99$ eV). Nevertheless, the high oxidative potential of photogenerated holes at VB of nsg-C_3N_4 enables simultaneous direct oxidation and degradation of MB [40]. Therefore the possible mechanism for photodegradation of MB could be proposed as follows [39]:

Absorption of efficient photons ($hv \geq E_g = 2.68$ eV) by nsg-C_3N_4 (Eq. 3). Direct oxidation of MB is possible due to the high oxidation potential of the hole (h^+_{VB}) on nsg-C_3N_4 (Eq. 4).

$$nsg - C_3N_4 + hv \rightarrow nsg - C_3N_4(e^-_{CB} + h^+_{VB}) \quad (3)$$

$$h^+_{VB} + MB \rightarrow Degradation\ product \quad (4)$$

In contrast, CB position of nsg-C_3N_4 is more negative than the reduction potential ($O_2/^{\cdot}O_2^-$) $= -0.33$ eV vs NHE as reported by [39]. Therefore, molecular oxygen (O_2) can be reduced to superoxide radicals ($^{\cdot}O_2^-$) by photogenerated electron of nsg-C_3N_4 (e_{CB}^-) (Eq. 5).

$$e^-_{CB} + O_2 \rightarrow \bullet O_2^- \quad (5)$$

$$\bullet O_2^- + H^+ \rightarrow \bullet HO_2^- \quad (6)$$

$$\bullet HO_2^- + MB \rightarrow \text{Degradation Product} \quad (7)$$

$$\bullet O_2^- + 2H^+ + e^-_{CB} \rightarrow H_2O_2 \quad (8)$$

$$H_2O_2 + MB \rightarrow \text{Degradation Product} \quad (9)$$

The produce superoxide radicals ($^{\cdot}O_2^-$) might also react with H^+ to form ($^{\cdot}HO_2^-$) and H_2O_2 (Eqs. 6 & 8) that are capable to degrade MB (Eqs. 7 & 9). Besides, the strong adsorption of MB on nsg-C_3N_4 could be attributed to strong π–π interaction between MB and nsg-C_3N_4 that causes MB and solid photocatalyst to be strongly held together. Fundamentally, MB is a cationic dye molecule in nature, and evidence from FTIR spectra (Fig. 7) shows that nsg-C_3N_4 has unique properties of delocalised π electrons in the s-heptazine ring and it also consists of terminal N atom with lone pair of electrons. Therefore, the strong interaction at solid–dye interface is due to cationic–columbic interaction of MB and nsg-C_3N_4 [41].

Langmuir–Hinshelwood model is widely applied for analysis of photocatalytic degradation kinetics of pollutant in aqueous phase [42,43]. To describe the photodegradation kinetics of MB, Langmuir–Hinshelwood model as expressed in the following Eq. 10 was employed:

$$r_o = -\frac{dC}{dt} = \frac{kKC}{1 + KC} \quad (10)$$

where r_o is the initial rate of reaction (mg/L.min), C is the concentration of pollutant (mg/L), t is the reaction time (min), k is the Langmuir–Hinshelwood reaction rate constant (mg/L.min), and K is the Langmuir adsorption equilibrium constant (L/mg). At a relatively weak adsorption or at a diluted concentration of pollutant, Eq. 10 could be assumed and simplified to be pseudofirst-order kinetics model as shown in Eq.

11. This equation was further integrated between the limits $C = C_o$ at $t = 0$, $C = C_e$ at t = ∞ and $C = C_t$ at $t = t$ to obtain a new expression in Eq. 12:

$$r_o = \frac{dC}{dt} = -kKC = -k_{app}C \tag{11}$$

$$C_t = (C_o - C_e)exp^{-k_{app}t} + C_e \tag{12}$$

where k_{app} is the apparent rate constant (min^{-1}), C_o is the initial concentration of pollutant, and C_e and C_t are the concentrations of pollutant at equilibrium and at respective contact time, respectively.

The experimental data for photodegradation of MB in aqueous solution were fitted to the nonlinearised pseudo-first-order kinetic model as shown in Fig. 8a and b. Rearranging Eq. 11 and Eq. 12 yields the nonlinearised pseudo-first-order kinetic model (Eq. 13):

$$R = R_e(1 - exp^{-k_{app}t}) \tag{13}$$

where R = MB removal (%) and $R_e = \left[\frac{C_o - C_e}{C_o} \times 100\right]$ is the percentage of MB removal at equilibrium. Based on the fitted nonlinearised pseudo-first-order model, the apparent rate constant, k_{app} (min^{-1}) can be determined quantitively.

All the parameters for pseudo-first-order kinetic models obtained are shown in Table 2. The nsg-C_3N_4 exhibited the fastest reaction at with the apparent rate constant (k_{app}) of 0.0202 min^{-1} compared to photolysis and bg-C_3N_4 at 0.0037 and 0.0166 min^{-1}, respectively. The R_e values obtained for bg-C_3N_4 (74.49%) and nsg-C_3N_4 (82.04%) are approximately close to the experimental data at 300 min, indicating that MB photodegradation process reached the equilibrium.

The powder g-C_3N_4 was separated using 10 min centrifugation at 3000 rpm before measuring the absorbance of the solution since both bg-C_3N_4 and nsg-C_3N_4 are fine powder that dispersed well in the MB solution. Knowing that it is inconvenient for the practical application of MB removal, a liquid-permeable self-supporting nanofibre with embedded g-C_3N_4 photocatalysts that can be handled manually was produced in this study. This form of photocatalyst is effective to recover catalyst from a treated solution compared to a dispersed powder sample. Fig. 8b compares the degradation of MB by NFbg-C_3N_4 and NFnsg-C_3N_4 as well as bare PAN nanofibres.

The results demonstrate that NFnsg-C_3N_4 performed the highest degradation of MB at 97.3% after 300 min. This excellent degradation resulted from the synergetic effects of adsorption by PAN nanofibres and degradation by nsg-C_3N_4 embedded in PAN nanofibres. The lower band gap with less electron recombination than NFbg-C_3N_4 allowed NFnsg-C_3N_4 to effectively degrade MB with high removal. Owing to the high surface area, both g-C_3N_4 nanofibres provided more photocatalytic active sites and produced more hydroxyl radicals and superoxide radical anions to improve the degradation of MB compared to the powder g-C_3N_4. This finding correlates with the statement that efficiency of dye degradation depends on the particle size and morphology of the photocatalyst [44]. The result also confirms that g-C_3N_4 embedded in PAN nanofibres showed sufficient photocatalytic activity, similar with the result showed by g-C_3N_4 that directly dispersed in a suspension solution. Meanwhile, 65.5% of MB was adsorbed using bare PAN nanofibres after 300 min, mainly attributed by the adsorption action by the PAN nanofibres. Although in real photocatalysis process, 300 min of photodegradation would take a longer time to complete and achieve 97.3% removal of MB, the prepared NFnsg-C_3N_4 showed a decent removal at ~90% after 120 min of photodegradation process compared to previous studies. In comparison, the MB photodegradation using g-C_3N_4 photocatalysts only obtained 62.6% of MB removal after 120 min [45]. Meanwhile, in another study, the MB removal with g-C_3N_4 was found at ~70% after 120 min of photodegradation under visible light irradiation [46].

Table 2
Removal of methylene blue (MB) under visible light irradiation and parameters for the pseudo-first-order kinetic model of the as-prepared samples.

Sample	Experimental Data	Parameters for pseudo-first-order kinetic model	
	MB removal (%)	R_e (%)	k_{app} (min^{-1})
Photolysis	23.9	33.93 ± 6.34	0.0037
bg-C_3N_4	77.6	74.49 ± 1.88	0.0166
nsg-C_3N_4	85.1	82.04 ± 1.98	0.0202
PAN nanofibre	65.5	61.99 ± 3.15	0.0145
NFbg-C_3N_4	90.8	87.82 ± 1.94	0.0269
NFnsg-C_3N_4	97.3	94.40 ± 2.23	0.0424

Although without the embedment of g-C_3N_4 in PAN nanofibres, the removal of MB gradually increased most probably not because of photodegradation but due to the adsorption of MB molecules into PAN nanofibres. However, PAN nanofibres can only assist in adsorption process of MB. PAN nanofibres without g-C_3N_4 is not useful for MB removal because it can finally lose adsorption capacity due to saturation. Photodegradation by g-C_3N_4 has a role in insitu removal of adsorbed MB by chemical decomposition, which is useful for continuous MB removal operation. Moreover, PAN polymer does not have photodegradation ability because it has no optical absorption at visible wavelength range. With respect to microstructures of nanofibre mats that have a network of highly well interconnected open pore with the size of several micrometres, the MB molecules were likely to be small enough to permeate in the nanofibre mat. Moreover, the MB molecules could sometimes collide with PAN nanofibres and eventually adsorbed in the nanofibre due to favourable affinity of MB molecules to PAN polymers. During electrospinning process to produce PAN nanofibres, large free volume between polymer chains of PAN was plausibly developed because of the rapid evaporation of solvent that caused polymer conformation to be frozen in nonequilibrium state [47,48]. Moreover, Freeman and Yampollskii [49] also mentioned that diffusion rates of small molecules increase with excess free volume of a polymer matrix. Therefore, the small diameter and excess volume in nanofibre potentially facilitate rapid molecular diffusion of MB molecules in the whole surface of nanofibres. According to Samitsu et al. [50], the excess volume also enhanced the absorption due to Langmuir-type adsorption site of MB molecules. Alias et al. [28] also reported that PAN nanofibres revealed excellent oil adsorption capability of nanofibres by increasing the concentration of oil species more than 300 times.

Based on the nonlinearised pseudo-first-order kinetic model fittings, NFnsg-C_3N_4 showed the fastest reaction with the apparent rate constant (k_{app}) of 0.0424 min^{-1} compared to bare PAN nanofibre and NFbg-C_3N_4 at 0.0145 and 0.0269 min^{-1}, respectively. Meanwhile, the R_e values obtained for bare PAN nanofibre (61.99%), NFbg-C_3N_4 (87.82%), and NFnsg-C_3N_4 (94.40%) only differ less than 5% from the experimental data at 300 min, demonstrating that all the photodegradation reactions reached equilibrium before 300 min.

The overall findings prove that g-C_3N_4 embedded PAN nanofibres can be considered as a potential candidate for dye removal with significant removal efficiency. The photocatalytic activity and removal efficiency of g-C_3N_4 and nanofibres increased in the order of bg-C_3N_4 < nsg-C_3N_4 < NFbg-C_3N_4 < NFnsg-C_3N_4. The summary for the degradation of MB under visible light irradiations and parameters for pseudo-first-order kinetic model of the as-prepared samples is presented in Table 2. Also, the comparison on the reported literature relating on the photodegradation of methylene blue (MB) and Rhodamine B (RhB) under visible light irradiation using various g-C_3N_4 and nanofibres photocatalysts is presented in Table 3.

4. Conclusions

A green facile synthesis of urea formed graphitic carbon nitride (bg-C_3N_4) photocatalyst and further liquid exfoliation done on g-C_3N_4 successfully transformed bg-C_3N_4 into nanosheet graphitic carbon

Table 3
Comparison on the photodegradation of methylene blue (MB) and Rhodamine B (RhB) under visible light irradiation using various graphitic carbon nitride (g-C_3N_4) powders and nanofibres photocatalysts.

Photocatalyst	Type	Photo-catalyst dosage (mg)	Light source (W)	Model dye	Initial concentration (mg/L)	Reaction Time (min)	Removal (%)	References
NFnsg-C_3N_4	Nanofibre mesh	200	30, LED	MB	10	300	97.3	This study
$BiFeO_3$/PVP	Nanofibre mesh	5	Natural sunlight	MB	0.01	240	96.0	[51]
$BiVO_4$/Pg-C_3N_4	Powder	30	50, LED	MB	20	60	90.0	[52]
B/g-C_3N_4/ZS	Powder	300	500, Xenon	MB	0.12 mmol/L	120	84.3	[35]
g-C_3N_4/PANI	Powder	25	500, Xenon	MB	10	30	78.6	[53]
g-C_3N_4/$CeVO_4$	Powder	10	500, Xenon	MB	0.01 mmol/L	210	75.0	[54]
g-C_3N_4/TiO_2	Powder	30	200, Xenon	MB	20	160	92.0	[55]
g-C_3N_4	Powder (nanofibre precursor)	100	350, Xenon	MB	10	120	90.9	[56]
TiO_2/g-C_3N_4	Powder (nanofibre precursor)	20	Natural sunlight	RhB	10	40	91.3	[57]
g-C_3N_4/PAN	Nanofibre mesh	1.5 × 1.5 mm	100, Visible light lamp	RhB	0.02 mmol/L	420	~97.0	[12]

nitride (nsg-C_3N_4) without any chemical reaction involved. The g-C_3N_4 photocatalysts were embedded into PAN nanofibres using electrospinning technique and formed nonwoven nanofibre mats that have excellent features such as high specific surface area, nodules nanofibres shape, and self-supported sheet which is easy to handle manually. g-C_3N_4 and nanofibres can photodegrade MB species under visible light irradiation. The degradation of MB was found at 77.6% using bg-C_3N_4 and the degradation improved to 85.1% using nsg-C_3N_4. The PAN nanofibre was found to effectively adsorb MB species inside the nanofibres. Most notably, the nsg-C_3N_4 incorporated into nanofibres exhibited MB degradation of 97.3% under visible light irradiation which is the highest value recorded in this study. The synergetic effects of concentration and degradation of MB species are the important factors for high photodegradation efficiency of MB, suggesting that NFnsg-C_3N_4 can be a better option for the treatment application of wastewater containing MB.

Declaration of Competing Interest

None.

Acknowledgements

This work was supported by the Malaysia Ministry of Higher Education, FRGS Research Grant (FRGS/1/2019/TK02/UITM/02/17), UTM-HiCOE Research Grants (R.J090301.7846.4J184 and R.J090301.7846.4J185), UTM Research University Grant (GUP) Tier 1 (Q.J130000.254616H43), Japan government for the Kurita Water and Environmental Foundation (KWEF) research grant (18P001), and Ministry of Education, Culture, Sports, Science and Technology (MEXT), Japan, Nanotechnology Platform (A-17-NM-0208). N.H.A. would like to thank Universiti Teknologi Malaysia (UTM)–National Institute for Materials Science (NIMS) Cooperative Graduate School Program (ICGP) 2017/18 for the graduate fellowship awarded. N.H.A. and S.S. would like to thank Dr. Takeshi Yasuda for his guidance on the photoluminescence measurements and Dr. Masanobu Naito from NIMS for his kind support.

References

[1] F. Goettmann, A. Fischer, M. Antonietti, A. Thomas, Chemical synthesis of mesoporous carbon nitrides using hard templates and their use as a metal-free catalyst for Friedel-Crafts reaction of benzene, Angew. Chem. Int. Ed. 45 (2006) 4467–4471, https://doi.org/10.1002/anie.200600412.

[2] S. Cao, J. Low, J. Yu, M. Jaroniec, Polymeric photocatalysts based on graphitic carbon nitride, Adv. Mater. 27 (2015) 2150–2176, https://doi.org/10.1002/adma.201500033.

[3] X. Zhang, X. Xie, H. Wang, J. Zhang, B. Pan, Y. Xie, Enhanced photoresponsive ultrathin graphitic-phase C3N4 nanosheet for bioimaging, J. Am. Chem. Soc. 135 (2013) 18–21, https://doi.org/10.1039/C5TA00402K.

[4] W.J. Ong, L.L. Tan, Y.H. Ng, S.T. Yong, S.P. Chai, Graphitic carbon nitride (g-C3N4)-based photocatalysts for artificial photosynthesis and environmental remediation: are we a step closer to achieving sustainability? Chem. Rev. 116 (2016) 7159–7329, https://doi.org/10.1021/acs.chemrev.6b00075.

[5] W. Iqbal, C. Dong, M. Xing, X. Tan, J. Zhang, Eco-friendly one-pot synthesis of well-adorned mesoporous g-C3N4 with efficiently enhanced visible light photocatalytic activity, Catal. Sci. Technol. 7 (2017) 1726–1734, https://doi.org/10.1039/C7CY00286F.

[6] C. Zhang, Y. Li, D. Shuai, Y. Shen, W. Xiong, L. Wang, Graphitic carbon nitride (g-C_3N_4)-based photocatalysts for water disinfection and microbial control: a review, Chemosphere 214 (2019) 462–479, https://doi.org/10.1016/j.chemosphere.2018.09.137.

[7] A. Sudhaik, P. Raizada, P. Shandilya, D. Jeong, J. Lim, Review on fabrication of graphitic carbon nitride based ef fi cient nanocomposites for photodegradation of aqueous phase organic pollutants, J. Ind. Eng. Chem. 67 (2018) 28–51.

[8] N.H. Alias, J. Jaafar, S. Samitsu, N. Yusof, M.H.D. Othman, M.A. Rahman, A.F. Ismail, F. Aziz, W.N.W. Salleh, N.H. Othman, Photocatalytic degradation of oilfield produced water using graphitic carbon nitride embedded in electrospun polyacrylonitrile nanofibers, Chemosphere 204 (2018) 79–86, https://doi.org/10.1016/j.chemosphere.2018.04.033.

[9] X. Kang, Y. Kang, X. Hong, Z. Sun, C. Zhen, C. Hu, Progress in natural science : materials international improving the photocatalytic activity of graphitic carbon nitride by thermal treatment in a high-pressure hydrogen atmosphere, Prog. Nat. Sci. Mater. Int. 28 (2018) 183–188, https://doi.org/10.1016/j.pnsc.2018.02.006.

[10] S. Yang, Y. Gong, J. Zhang, L. Zhan, L. Ma, Z. Fang, X. Wang, P.M. Ajayan, Exfoliated graphitic carbon nitride nanosheets as efficient catalysts for hydrogen evolution under visible light, J. Adv. Mater. 25 (2013) 2452–2456, https://doi.org/10.1002/adma.201204453.

[11] N.A.M. Nor, J. Jaafar, A.F. Ismail, M.A. Rahman, M.H.D. Othman, T. Matsuura, F. Aziz, N. Yusof, W.N.W. Salleh, M.N. Subramaniam, Effects of heat treatment of TiO2 nanofibers on the morphological structure of PVDF nanocomposite membrane under UV irradiation, J. Water Process Eng. 20 (2017) 193–200, https://doi.org/10.1016/j.jwpe.2017.11.007 Received.

[12] T. Xu, F. Wu, Y. Gu, Y. Chen, J. Cai, W. Lu, H. Hu, Z. Zhu, W. Chen, Visible-light responsive electrospun nanofibers based on polyacrylonitrile-dispersed graphitic carbon nitride, RSC Adv. 5 (2015) 86505–86512, https://doi.org/10.1039/c5ra15973c.

[13] R. Al-Attabi, Y. Morsi, J.A. Schütz, L.F. Dumée, One-pot synthesis of catalytic molybdenum based nanocomposite nano-fiber membranes for aerosol air remediation, Sci. Total Environ. 647 (2019) 725–733, https://doi.org/10.1016/j.scitotenv.2018.08.050.

[14] R. Al-Attabi, J. Rodriguez-Andres, J.A. Schütz, M. Bechelany, E. des Ligneris, X. Chen, L. Kong, Y.S. Morsi, L.F. Dumée, Catalytic electrospun nano-composite membranes for virus capture and remediation, Sep. Purif. Technol. 229 (2019) 115806, , https://doi.org/10.1016/j.seppur.2019.115806.

[15] A. Liyana, N. Hanis, H. Hairom, L. Yong, C. Yin, M. Khairul, A. Wahab, Industrial textile wastewater treatment via membrane photocatalytic reactor (MPR) in the presence of ZnO-PEG nanoparticles and tight ultra fi ltration, J. Water Process Eng. 31 (2019) 100872, , https://doi.org/10.1016/j.jwpe.2019.100872.

[16] A. Ameta, R. Ameta, M. Ahuja, Photocatalytic degradation of methylene blue over ferric tungstate, Sci. Rev. Chem. Commun. 3 (2013) 172–180.

[17] S. Saroj, K. Kumar, N. Pareek, R. Prasad, R.P. Singh, Biodegradation of azo dyes Acid Red 183, Direct Blue 15 and Direct Red 75 by the isolate Penicillium oxalicum SAR-3, Chemosphere 107 (2014) 240–248, https://doi.org/10.1016/j.chemosphere.2013.12.049.

[18] N.H. Othman, N.H. Alias, M.Z. Shahruddin, N.F. Abu Bakar, N.R. Nik Him, W.J. Lau, Adsorption kinetics of methylene blue dyes onto magnetic graphene oxide, J. Environ. Chem. Eng. 6 (2018) 2803–2811, https://doi.org/10.1016/j.jece.2018.04.024.

[19] R. Gharibshahi, A. Jafari, H. Ahmadi, CFD investigation of enhanced extra-heavy oil recovery using metallic nanoparticles / steam injection in a micromodel with random pore distribution, J. Pet. Sci. Eng. 174 (2019) 374–383, https://doi.org/10.1016/j.petrol.2018.10.051.

[20] N. Hanis, H. Hairom, A. Wahab, A. Amir, H. Kadhum, Nanofiltration of hazardous Congo red dye : performance and flux decline analysis, J. Water Process Eng. 4 (2014) 99–106.

[21] U. Tahir, A. Yasmin, U.H. Khan, Phytoremediation: potential flora for synthetic dyestuff metabolism, J. King Saud Univ. Sci. 28 (2016) 119–130, https://doi.org/10.1016/j.jksus.2015.05.009.

[22] E. Ozturk, N.C. Cinperi, Water efficiency and wastewater reduction in an integrated woolen textile mill, J. Clean. Prod. 201 (2018) 686–696, https://doi.org/10.1016/j.jclepro.2018.08.021.

[23] M. Ali, Q. Husain, N. Alam, M. Ahmad, Nano-peroxidase fabrication on cation exchanger nanocomposite: augmenting catalytic efficiency and stability for the decolorization and detoxification of Methyl Violet 6B dye, Sep. Purif. Technol. 203 (2018) 20–28, https://doi.org/10.1016/j.seppur.2018.04.012.

[24] R.T. Thomas, N. Sandhyarani, Template free synthesis of graphitic carbon nitride/titania mesoflowers, RSC Adv. (2015) 72683–72690, https://doi.org/10.1039/c5ra14547c.

[25] M.N. Subramaniam, P.S. Goh, N. Abdullah, W.J. Lau, B.C. Ng, A.F. Ismail, Adsorption and photocatalytic degradation of methylene blue using high surface area titanate nanotubes (TNT) synthesized via hydrothermal method, J. Nanopart. Res. 19 (2017) 1–13, https://doi.org/10.1007/s11051-017-3920-9.

[26] S. Wong, N. Ngadi, I.M. Inuwa, O. Hassan, Recent advances in applications of activated carbon from biowaste for wastewater treatment: a short review, J. Clean. Prod. 175 (2018) 361–375, https://doi.org/10.1016/j.jclepro.2017.12.059.

[27] T.M. Elmorsi, Equilibrium isotherms and kinetic studies of removal of methylene blue dye by adsorption onto miswak leaves as a natural adsorbent, J. Environ. Prot. (Irvine,. Calif) 2 (2011) 817–827, https://doi.org/10.4236/jep.2011.26093.

[28] N.H. Alias, J. Jaafar, S. Samitsu, N. Yusof, M.H.D. Othman, M.A. Rahman, A.F. Ismail, F. Aziz, W.N.W. Salleh, N.H. Othman, Photocatalytic degradation of oilfield produced water using graphitic carbon nitride embedded in electrospun polyacrylonitrile nanofibers, Chemosphere 204 (2018) 79–86, https://doi.org/10.1016/j.chemosphere.2018.04.033.

[29] N.H. Alias, J. Jaafar, S. Samitsu, T. Matsuura, A.F. Ismail, S. Huda, N. Yusof, F. Aziz, Photocatalytic nanofiber-coated alumina hollow fiber membranes for highly efficient oilfield produced water treatment, Chem. Eng. J. 360 (2019) 1437–1446, https://doi.org/10.1016/j.cej.2018.10.217.

[30] T.Y. Ma, Y. Tang, S. Dai, S.Z. Qiao, Proton-functionalized two-dimensional graphitic carbon nitride nanosheet: an excellent metal-/label-free biosensing platform, Small 10 (2014) 2382–2389, https://doi.org/10.1002/smll.201303827.

[31] Q. Liang, Z. Li, Y. Bai, Z.-H. Huang, F. Kang, Q.-H. Yang, Reduced-sized monolayer carbon nitride nanosheets for highly improved photoresponse for cell imaging and photocatalysis, Sci. China Mater. 60 (2017) 109–118, https://doi.org/10.1007/s40843-016-5131-9.

[32] M.J. Lima, P.B. Tavares, A.M.T. Silva, C.G. Silva, J.L. Faria, Selective photocatalytic oxidation of benzyl alcohol to benzaldehyde by using metal-loaded g-C3N4 photocatalysts, Catal. Today 287 (2017) 70–77, https://doi.org/10.1016/j.cattod.2016.11.023.

[33] S. Tonda, S. Kumar, S. Kandula, V. Shanker, Fe-doped and -mediated graphitic carbon nitride nanosheets for enhanced photocatalytic performance under natural sunlight, J. Mater. Chem. A 2 (2014) 6772–6780, https://doi.org/10.1039/c3ta15358d.

[34] Y. Xu, Y. Gong, H. Ren, W. Liu, L. Niu, C. Li, X. Liu, In situ structural modification of graphitic carbon nitride by alkali halides and influence on photocatalytic activity, RSC Adv. 7 (2017) 32592–32600, https://doi.org/10.1039/C7RA05555B.

[35] W. Tian, Q. Shen, N. Li, J. Zhou, Efficient degradation of methylene blue over boron-doped g-C3N4/Zn0.8Cd0.2S photocatalysts under simulated solar irradiation, RSC Adv. 6 (2016) 25568–25576, https://doi.org/10.1039/C6RA01429A.

[36] P.V. Gulgunje, B.A. Newcomb, K. Gupta, H.G. Chae, T.K. Tsotsis, S. Kumar, Low-density and high-modulus carbon fibers from polyacrylonitrile with honeycomb structure, Carbon N. Y. 95 (2015) 710–714, https://doi.org/10.1016/j.carbon.2015.08.097.

[37] W. Pan, X. He, Y. Chen, Preparation and characterization of polyacrylonitrile/antimony doped tin oxide composite nanofibers by electrospinning method, Optoelectron. Adv. Mater. Rapid Commun. 4 (2010) 390–394.

[38] Y. Yang, J. Chen, Z. Mao, N. An, Ultrathin g-C_3N_4 nanosheets with an extended visible-light-responsive range for significant enhancement of photocatalysis, RSC Adv. 7 (2017) 2333–2341, https://doi.org/10.1039/c6ra26172h.

[39] M. Azuwa, M.F.M. Zain, L. Je, M.B. Kassim, N. Aishah, S. Amin, W.N.W. Salleh, M. Nur, I. Salehmin, M. Faizal, Z. Adlan, M. Hir, Constructing bio-templated 3D porous microtubular C-doped g-C3N4 with tunable band structure and enhanced charge carrier separation, Appl. Catal. B Environ. 236 (2018) 265–279.

[40] Z. Jiang, C. Zhu, W. Wan, K. Qian, J. Xie, Constructing graphite-like carbon nitride modified hierarchical yolk–shell TiO2 spheres for water pollution treatment and hydrogen production, J. Mater. Chem. A. 4 (2016) 1806–1818, https://doi.org/10.1039/C5TA09919F.

[41] B. Choudhury, P.K. Giri, Isotype heterostructure of bulk and nanosheets of graphitic carbon nitride for efficient visible light photodegradation of methylene blue, RSC Adv. 6 (2016) 24976–24984, https://doi.org/10.1039/C6RA00933F.

[42] K.V. Kumar, K. Porkodi, F. Rocha, Langmuir-Hinshelwood kinetics - A theoretical study, Catal. Commun. 9 (2008) 82–84, https://doi.org/10.1016/j.catcom.2007.05.019.

[43] M. Azuwa, J. Jaafar, M.F.M. Zain, L. Jeffery, M.B. Kassim, M. Saufi, N. Hashimah, In-depth understanding of core-shell nanoarchitecture evolution of g-C3N4@C,N co-doped anatase/rutile: efficient charge separation and enhanced visible-light photocatalytic performance, Appl. Surf. Sci. 436 (2018) 302–318.

[44] C. Valero-luna, S.A. Palomares-sanchéz, F. Ruíz, Catalytic activity of the barium hexaferrite with H2O2/visible light irradiation for degradation of methylene blue, Catal. Today 266 (2016) 110–119.

[45] D.R. Paul, R. Sharma, S.P. Nehra, A. Sharma, Effect of calcination temperature, pH and catalyst loading on photodegradation efficiency of urea derived graphitic carbon nitride towards methylene blue dye solution, RSC Adv. (2019) 15381–15391, https://doi.org/10.1039/c9ra02201e.

[46] D. Fu, G. Han, F. Liu, Y. Xiao, H. Wang, R. Liu, C. Liu, Visible-light enhancement of methylene blue photodegradation by graphitic carbon nitride- titania composites, Mater. Sci. Semicond. Process. 27 (2014) 966–974, https://doi.org/10.1016/j.mssp.2014.08.004.

[47] M. Makaremi, R.T. De Silva, P. Pasbakhsh, Electrospun nanofibrous membranes of polyacrylonitrile/halloysite with superior water filtration ability, J. Phys. Chem. C 119 (2015) 7949–7958, https://doi.org/10.1021/acs.jpcc.5b00662.

[48] L.H. Sperling, Introduction to Physical Polymer Science, John Wiley & Sons, Inc., Hoboken, New Jersey, 2005, https://doi.org/10.1002/0471757128.ch10.

[49] B. Freeman, Y. Yampollskii, Membrane Gas Separation, John Wiley & Sons, Ltd., Chichester, United Kingdom, 2010, https://doi.org/10.1002/9780470665626.

[50] S. Samitsu, R. Zhang, X. Peng, M.R. Krishnan, Y. Fujii, I. Ichinose, Flash freezing route to mesoporous polymer nanofibre networks, Nat. Commun. 4 (2013) 1–7, https://doi.org/10.1038/ncomms3653.

[51] S. Bharathkumar, M. Sakar, R.V. K, S. Balakumar, Versatility of electrospinning in the fabrication of fibrous mat and mesh nanostructures of bismuth ferrite (BiFeO3) and their magnetic and photocatalytic activities, Phys. Chem. Chem. Phys. 17 (2015) 17745–17754, https://doi.org/10.1039/C5CP01640A.

[52] Z. Wang, J. Lv, J. Zhang, K. Dai, C. Liang, Facile synthesis of Z-scheme BiVO4/porous graphite carbon nitride heterojunction for enhanced visible-light-driven photocatalyst, Appl. Surf. Sci. 430 (2018) 595–602, https://doi.org/10.1016/j.apsusc.2017.06.093.

[53] S. Zhang, L. Zhao, M. Zeng, J. Li, J. Xu, X. Wang, Hierarchical nanocomposites of polyaniline nanorods arrays on graphitic carbon nitride sheets with synergistic effect for photocatalysis, Catal. Today 224 (2014) 114–121, https://doi.org/10.1016/j.cattod.2013.12.008.

[54] X.W. Li, Li, Haoran Wang, CeVO4 nanofibers hybridized with g-C3N4 nanosheets with enhanced visible-light-driven photocatalytic activity, Solid State Commun. 269 (2018) 11–15, https://doi.org/10.1016/j.ssc.2017.10.008.

[55] D. Fu, G. Han, F. Liu, Y. Xiao, H. Wang, R. Liu, C. Liu, Visible-light enhancement of methylene blue photodegradation by graphitic carbon nitride-titania composites, Mater. Sci. Semicond. Process. 27 (2014) 966–974, https://doi.org/10.1016/j.mssp.2014.08.004.

[56] M. Xie, W. Wei, Z. Jiang, Y. Xu, J. Xie, Carbon nitride nanowires/nanofibers: a novel template-free synthesis from a cyanuric chloride-melamine precursor towards enhanced adsorption and visible-light photocatalytic performance, Ceram. Int. 42 (2016) 4158–4170, https://doi.org/10.1016/j.ceramint.2015.11.089.

[57] S.P. Adhikari, G.P. Awasthi, H.J. Kim, C.H. Park, C.S. Kim, Electrospinning directly synthesized porous TiO2 nanofibers modified by graphitic carbon nitride sheets for enhanced photocatalytic degradation activity under solar light irradiation, Langmuir 32 (2016) 6163–6175, https://doi.org/10.1021/acs.langmuir.6b01085.